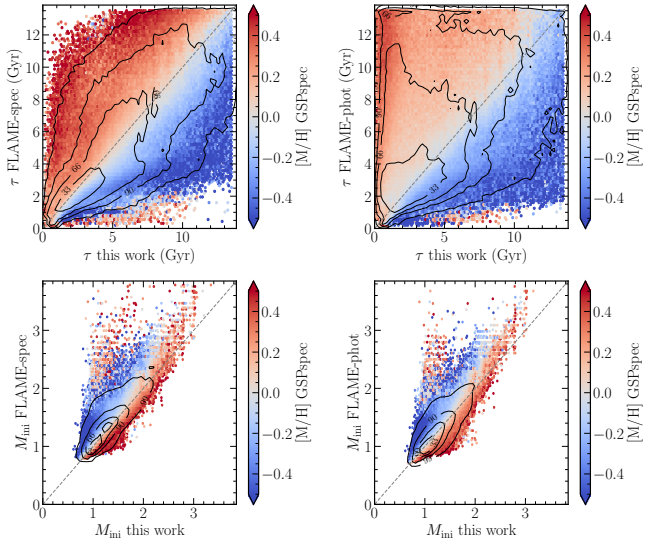

Fig. 12. Comparison of the ages (top) and the masses (bottom) between the estimations obtained in this work and with those of FLAME-Spec (left) and FLAME-Phot (right). Only GSP-Spec turn-off stars with the first 13 GSP-Spec flags equal to zero are selected here, with age uncertainties (both in our code and the FLAME modules) smaller than 50 per cent. Contour lines contain 33, 66, 90, and 99 per cent of the distribution. The colour-coding is the GSP-Spec calibrated [M/H].

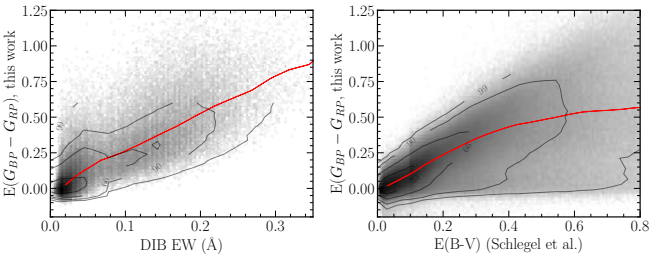

Fig. 13. Comparison of $E(G_{BP} - G_{RP})$ derived in this work, with the equivalent widths of diffuse interstellar bands at 862 nm derived from the same GSP-Spec spectra (left) and the Schlegel et al. (1998) $E(B-V)$ with the Bonifacio et al. (2000) correction (*right*). For both plots, the grey colour-scale is the logarithm of the number of stars in one bin, and the red lines represent the running median. Overall, the correlations in both cases are very good.

2.8. Calculation of the reddening and the extinction

To derive the extinctions it is first necessary to compute the reddening $E(G_{BP} - G_{RP})$, obtained by measuring the difference between the projected and the observed colours $(G_{BP} - G_{RP})$. Extinction, A_G, is then computed using

$$A_G = c_\theta \cdot E(G_{BP} - G_{RP}), \tag{9}$$

where c_θ is a constant that depends on the stellar type[11] (Creevey et al. 2023; Fouesneau et al. 2022).

The left plot of Fig. 13 compares the reddening $E(G_{BP} - G_{RP})$ derived in our work, with the equivalent widths of the diffuse interstellar band at ~862 nm, as derived in Gaia Collaboration (2023b). The right plot is a comparison with the Schlegel et al. (1998) $E(B-V)$ reddening (corrected as described in Sect. 2.6.2 towards the regions with the largest extinction).

[11] For extinction converters as a function of the passband and the stellar atmospheric parameters see https://www.cosmos.esa.int/web/gaia/dr3-astrophysical-parameter-inference

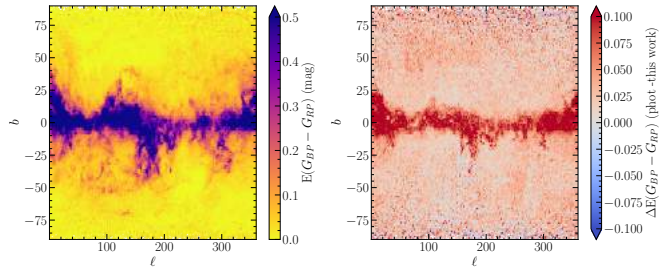

Fig. 14. Galactic (ℓ, b) maps of the $E(G_{BP} - G_{RP})$ distribution (left) and the residuals between the $E(G_{BP} - G_{RP})$ estimation from GSP-Phot and our values (right).

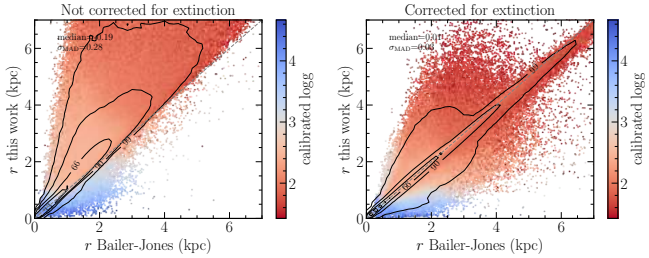

Fig. 15. Comparison of the line-of-sight distances derived from the projected M_G and extinction, with the geometric values from Bailer-Jones et al. (2021). No cuts in the uncertainties on the Bailer-Jones et al. (2021) distances or in our line-of-sight distances are made.

Overall, a good correlation is found with the two dust proxies, confirming our estimations of reddening. We note, however, that some of our targets have $E(G_{BP} - G_{RP})$ values lower than zero. We decided not to artificially put them equal to zero, but note that the associated uncertainties of these stars should be considered.

The left plot of Fig. 14 shows the reddening map derived for the sample. The right plot of the same figure shows the residuals between the GSP-Phot $E(G_{BP} - G_{RP})$ values and ours. The median difference above and below Galactic latitudes of $|b| = 20°$ is 0.019 mag and 0.052 mag, respectively. The agreement is rather good, acknowledging that GSP-Phot does not use the same input data or parameters as we do, and that it is precisely towards highly reddened regions that degeneracies between $E(BP - RP)$ and $T_{\rm eff}$ make the GSP-Phot parametrisation challenging.

2.9. Absolute magnitudes and line-of-sight distances

Finally, to validate more thoroughly the projected absolute magnitudes, we compare the geometric line-of-sight distances, r, of Bailer-Jones et al. (2021) with those derived via the distance modulus (correcting for the projected extinctions, assuming $c_\theta = 1.83037$, valid for solar-type stars ±1500 K). The results are shown in Fig. 15 (left, before correcting for the extinction, and right, after applying the correction). They suggest that we find a very good agreement between the two distance estimations, with a null median residual and a dispersion of 20 pc. We find that the one per cent of stars that have the largest disagreement with the Bailer-Jones et al. (2021) distances also have either large differences between the input $\log g$ and the projected one (>0.3) if these stars are dwarfs or large age uncertainties (larger than 50 per cent) if these stars are giants.

Finally, we note that the very good agreement that is found is not necessarily a direct consequence of the use of r when projecting the absolute magnitudes. We recall that when we project the absolute magnitudes, extinction is ignored. As can be seen in the left plot of this figure (which does not correct for the derived interstellar reddening), when the estimated A_G is neglected when computing the distance, the agreement between the two distance estimates is rather poor and biased.

3. Age and mass correlations with the orbital parameters and the positions in the Galaxy

In this section we illustrate the quality and the limitations of our projected parameters. To do so, we first compute the orbital parameters for all of the stars with measured radial velocities from the RVS and available astrometry. Then we correlate them with the stellar ages and masses for a high-quality GSP-Spec sample, requiring the first 12 quality flags of GSP-Spec to be smaller than or equal to one (except `fluxNoise_flag`, which we require to be smaller than or equal to 2); the `KMgiantPar_flag`, which we require equal to zero; and the relative age uncertainty, which we require to be smaller than 50 per cent.

3.1. Determination of galactocentric positions, velocities, and orbital parameters

The galactocentric positions X, Y, Z (in Cartesian coordinates), R (galactocentric cylindrical radius), and cylindrical velocities (radial V_R, azimuthal V_ϕ, vertical V_Z) in a right-handed frame were computed for all of the stars that have a *Gaia* radial velocity measured (~33 million targets). In order to do so, we used the star's right ascension, declination, line-of-sight velocity, proper motions, and Bailer-Jones et al. (2021) EGDR3 geometric and photogeometric Bayesian line-of-sight distances (therefore leading to two sets of positions, velocities, and orbits). The assumed solar position is $(R, Z)_\odot = (8.249, 0.0208)$ kpc (GRAVITY Collaboration 2020; Bennett & Bovy 2019), and the velocities are $(V_R, V_\phi, V_Z)_\odot = (-9.5, 250.7, 8.56)$ km s^{-1} (Reid & Brunthaler 2020; GRAVITY Collaboration 2020).

To compute the orbital parameters (actions, eccentricities, apocentre, pericentre, maximum distance from the Galactic plane), we used the Stäckel fudge method (Binney 2012; Sanders & Binney 2016; Mackereth & Bovy 2018) with the Galpy code (Bovy 2015), in combination with the axisymmetric potential of McMillan (2017) (adjusted to our adopted solar position and the local standard of rest velocity). The lower and upper confidence limits (corresponding to the 16th and 84th percentiles) were obtained by propagating the uncertainties of the line-of-sight distance, line-of-sight velocity, and proper motions using 20 Monte-Carlo realisations. No correlation between proper motions and distance uncertainties were taken into account, and we assumed a non-Gaussian distribution for r, constructed as two half-Gaussians defined by the upper and lower confidence limits of r.

3.2. Galactic maps of ages and masses and identification of the spiral arms

Maps of the stellar ages and masses in Galactic Aitoff projection (ℓ, b) are shown in Fig. 16. Young and massive stars are predominantly found in (or close to) the Galactic plane, within the regions of high reddening (see Fig. 14), as expected from the interstellar medium distribution in the Milky Way (e.g. Kalberla & Kerp 2009, and references therein).

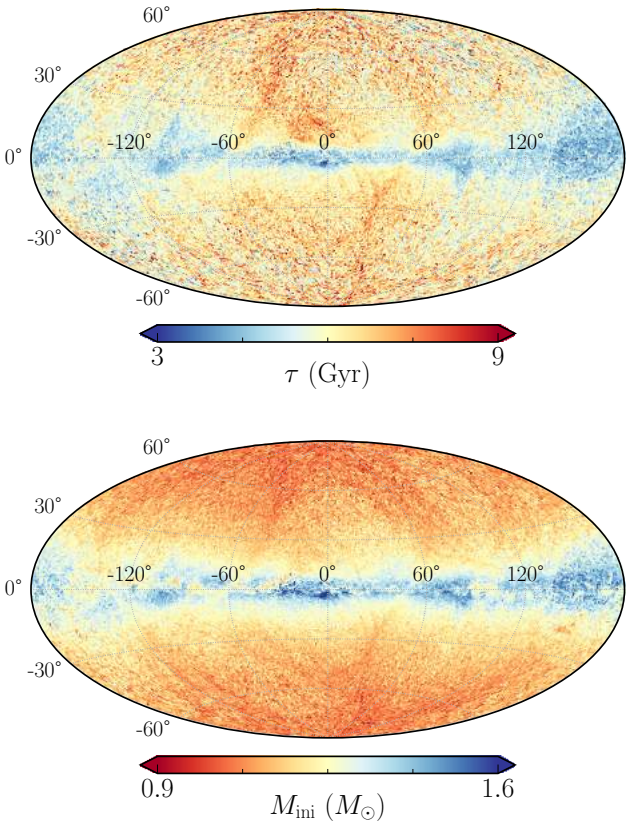

Fig. 16. Healpix projections (NSIDE=64) of the mean ages (top) and masses (bottom) for the compiled sample.

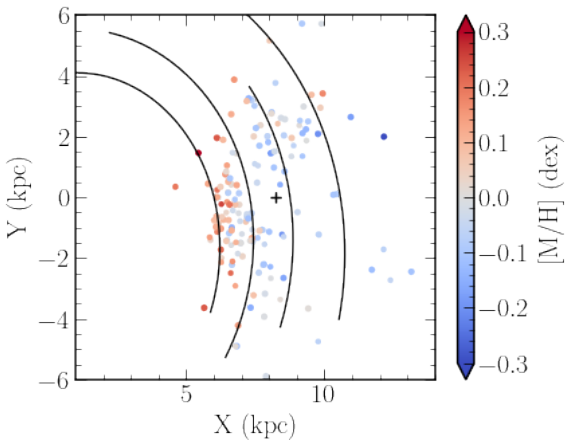

Fig. 17. Galactocentric Cartesian XY projection of the position of the stars having $M_{\rm ini} \geq 4\,M_\odot$, $\log g < 2$, and $Z_{\rm max} < 0.5$ kpc. The Galactic centre is located at $(X, Y) = 0$ (on the left) and Galactic rotation is going clockwise. The colour-coding represents the metallicity of the stars, whereas the plus sign is located at the Sun's position. The position of the Perseus, Local, Sagittarius, and Scutum spiral arms, based on the Castro-Ginard et al. (2021) results, are also plotted as black continuous lines.

In Fig. 17 we plot the galactocentric Cartesian X-Y positions of stars that have an estimated initial mass greater than 4 solar masses, $\log g < 2$ (to avoid massive main-sequence stars at the solar vicinity) and a maximum distance from the galactic plane during their orbit (i.e. $Z_{\rm max}$) less than 0.5 kpc. Superimposed,

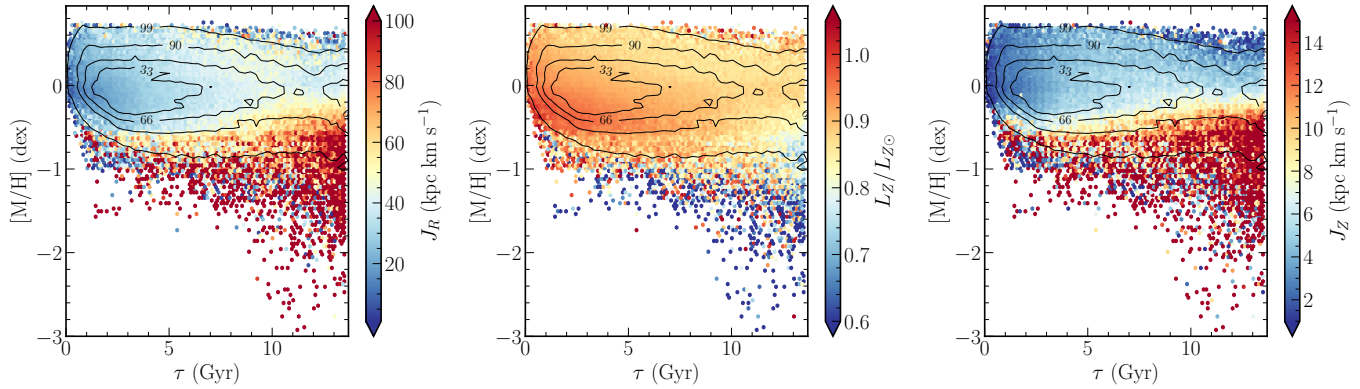

Fig. 18. Age-metallicity relations as a function of the radial and vertical actions (J_R, J_Z, first and third panel, respectively) and normalised angular momentum (L_Z normalised by the Sun's value, middle panel) for stars closer than 1 kpc from the Sun.

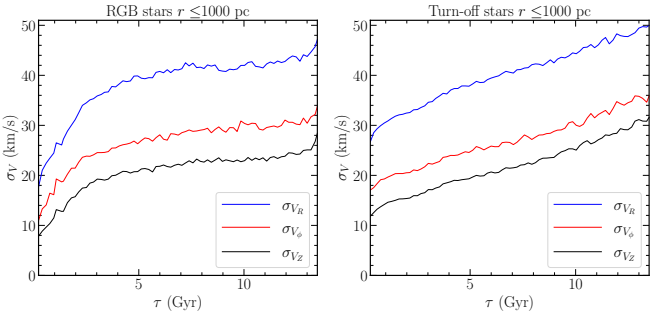

Fig. 19. Age-velocity dispersion for the RGB stars (*left*) and for the turn-off stars (*right*) closer than 1 kpc from the Sun. A clear trend is found in both samples, for each velocity component. However, the fact that these trends do not exhibit the same shape, highlights the different precisions achieved for each stellar type: RGB stars tend to have underestimated ages for old stars, whereas the younger turn-off stars tend to have overestimated ages.

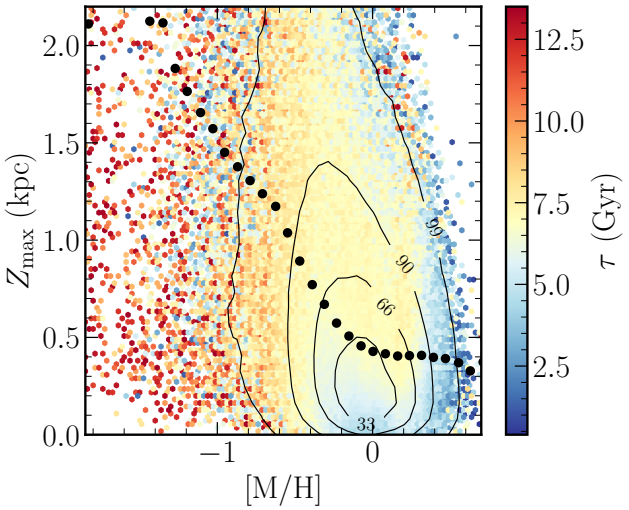

Fig. 20. Maximum distance from the Galactic plane reached during a star's orbit (Z_{max}, in kpc) vs. metallicity, colour-coded by age (in Gyr). A clear increase in Z_{max} as a function of metallicity and age can be seen from the black dots on the figure that represent the running mean. This trend is compatible with what is expected for a transition between thin and thick discs and between thick disc and halo.

we also plot the position of the Perseus, Local, Sagittarius, and Scutum spiral arms, based on the Castro-Ginard et al. (2021) analysis of open clusters with *Gaia* EDR3 data (adapted to match our assumed solar position). The positions of the massive stars follow very closely the positions of the modelled spiral arms, consistent with the fact that the latter are regions where star formation takes place. Furthermore, one can also see the clear metallicity gradient within those stars, reflecting the metallicity of the interstellar medium at these locations (as these stars are found to be younger than 300 Myr).

3.3. Age-metallicity relation as a function of orbital actions

Figure 18 shows the age metallicity-relation we derive for the stars within 1 kpc from the Sun, colour-coded by the three different computed actions. Overall, we find a flat trend over the entire age-range, in agreement with previous studies (e.g. Edvardsson et al. 1993; Casagrande et al. 2011; Bergemann et al. 2014; Feuillet et al. 2019). Young stars ($\tau \lesssim 2$ Gyr) of subsolar metallicity tend to have low J_R and $L_Z/L_{Z\odot}$ above one, compatible with stars visiting the solar neighbourhood on slightly eccentric orbits from the outer disc (we find that these stars have $e < 0.1$).

Super-solar metallicity stars are found at all ages, with perhaps a slight decrease in their number for ages above 10 Gyr that may be due to our age prior. However, it is worth noting that whereas the youngest super-solar metallicity stars have low J_R and $L_Z/L_{Z\odot}$ close to 0.9, the older stars have on average a larger radial action and more eccentric orbits ($e > 0.3$), suggesting that they just visit the solar neighbourhood, while being close to their apocentre. Interestingly, we also find old ($\tau > 8$ Gyr) metal-rich stars with normalised angular momentum around one and low values of radial and vertical actions. These stars are obvious candidates of objects having experienced churning processes, i.e. stars that moved far from their birthplace without changing their eccentricity via corotation resonances with the spiral arms or the Galactic bar (Schönrich & Binney 2009; Minchev et al. 2013; Kordopatis et al. 2015a).

Finally, we find that metal-poor stars ([M/H] < -1 dex) within 1 kpc from the Sun are predominantly old, with large radial and vertical actions and low angular momenta, as is expected for typical halo stars.

3.4. Age-velocity dispersion and Z_{max}-metallicity relations

Figure 19 shows the age-velocity dispersion relation of our RGB sample (left) and our turn-off sample (right), for stars closer

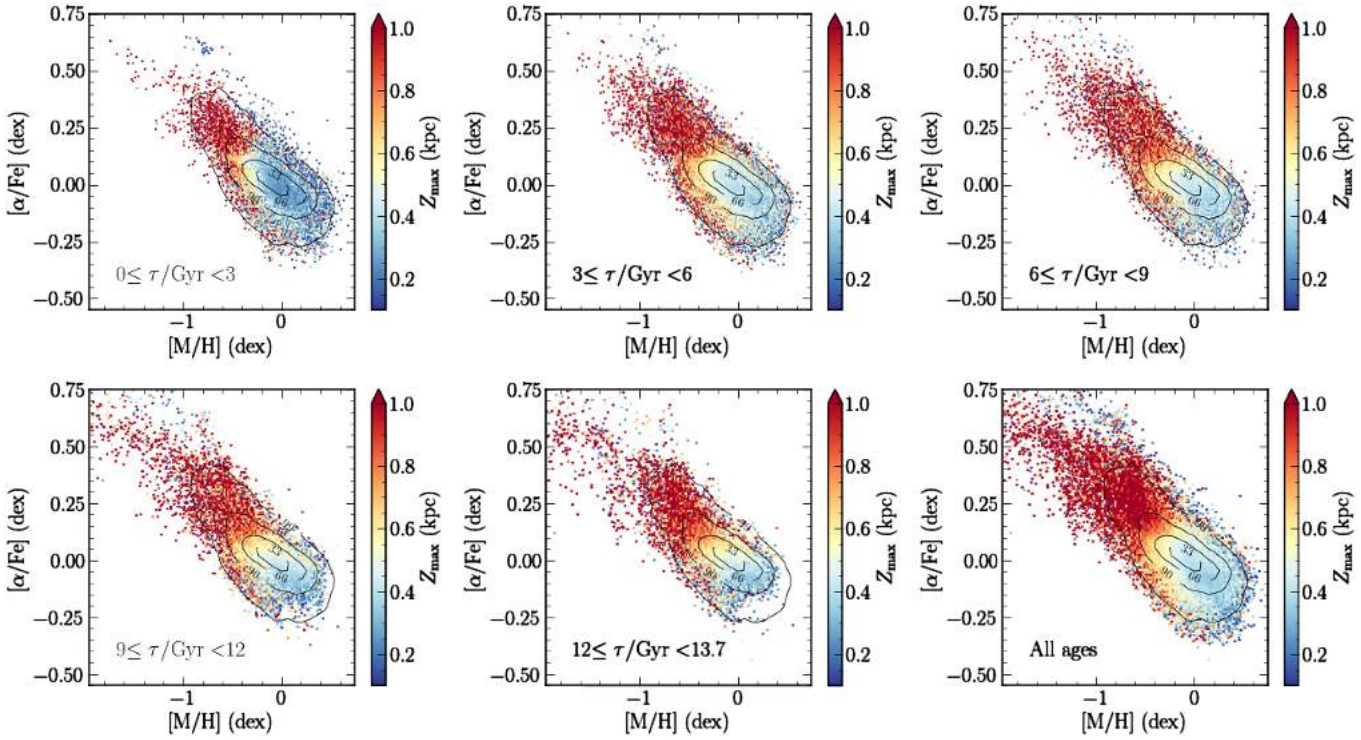

Fig. 21. Calibrated [α/Fe] vs. [M/H], in 3 Gyr age bins for giant stars ($\log g < 3.5$) closer than 1.5 kpc from the Sun. The contour lines inside each panel were evaluated for the sample considering all the age ranges, represented in the bottom right panel. The colour-coding corresponds to the maximum distance above the Galactic plane that a star can reach during its orbit.

than 1 kpc from the Sun. In agreement with previous results (e.g. Aumer & Binney 2009), we find a clear increase in the velocity dispersions with age, which is even more pronounced when selecting only the turn-off stars. The trend for old stars is starker for the turn-off sample, whereas the giants seem to have a stronger trend at the young side. These different behaviours are in agreement with those described in Sect. 2.7 using the APOKASC-2 and Casagrande et al. (2011) datasets, which suggests that old giants tend to have underestimated ages, whereas very young turn-off stars tend to have overestimated ages.

Similarly, Fig. 20 shows the maximum distance from the Galactic plane reached during a star's orbit as a function of metallicity, colour-coded by age. The black circles represent the running mean in bins of [M/H]. It can be seen that stars with metallicities greater than −0.2 dex tend to be young ($\tau < 5$ Gyr) and confined in a thin-disc configuration ($Z_{\rm max} < 0.3$ kpc), whereas stars with $-0.2 <$ [M/H] < -1 dex have $Z_{\rm max} < 1.1$ kpc and are globally younger than 10 Gyr, in agreement with the thick-disc properties in the solar neighbourhood (e.g. Bensby et al. 2014; Haywood et al. 2018).

3.5. Chemical enrichment of the Galactic disc

A different way to show the wealth of information in our sample can be seen in Fig. 21, where we plot the [α/Fe] − [M/H] space, in various age-bins, as a function of the orbital parameters (in this case, $Z_{\rm max}$). The [α/Fe] of GSP-Spec, being mostly based on calcium abundance, does not allow us to separate the well-known thin- and thick-disc chemical sequences (see e.g. Kordopatis et al. 2015b; Hayden et al. 2015, obtained with high-resolution *Gaia*-ESO or APOGEE spectra); nevertheless, one can see that young stars mostly have low [α/Fe] ratios (<0.2), high metallicity (> -0.5), and low $Z_{\rm max}$. As look-back time (i.e. age) increases, lower metallicity and higher [α/Fe] regions become populated, with the low-metallicity tail exhibiting the highest $Z_{\rm max}$ values. Chemical evolution models can then be fitted to these trends in order to determine the star formation history of the Galaxy together with its gas infall history.

In addition to the inner evolution of the Milky Way, our dataset also allows us to probe accreted populations present in the surveyed volume. For example, low-metallicity and low-[α/Fe] stars with high $Z_{\rm max}$ associated with *Gaia*-Enceladus-Sausage (Belokurov et al. 2018; Helmi et al. 2018) stars are detected starting from $\tau > 3$ Gyr (with possible traces even below that value, which we believe are subgiants with underestimated ages). Interestingly, the plot also shows some low-metallicity ([M/H] < -0.6 dex) α-enhanced ([α/Fe] > 0.55 dex) and low-$Z_{\rm max}$ (< 0.3 kpc) stars present at all age bins. We find that these stars are mostly targets with $T_{\rm eff} > 6000$ K and similar $\log g \sim 3.5$ (also seen in the top left plot of Fig. 9). The true existence of these targets will have to be investigated further.

4. Conclusions

Using the calibrated atmospheric parameters derived from *Gaia* spectra and the GSP-Spec module, the photometry from 2MASS and *Gaia*-EDR3, and Bayesian line-of-sight distances estimated using *Gaia*-EDR3 parallaxes, we derived the ages, initial masses, and absolute magnitudes for ∼5 million targets in four different ways, depending on different combinations of parameters to project on isochrones, and based on PARSEC isochrones. We propose a way to combine these different estimations based on the extinction along the line of sight (see Sect. 2.6.2), and publish a compiled catalogue of best projected parameters and their uncertainties.

We note that the reliability of the projected parameters is closely related to that of the input data and their associated

uncertainties. Biases in $T_{\rm eff}$, $\log g$, [M/H], or distance modulus, and/or underestimated errors on them, may lead (depending on the stellar evolutionary phase) to biases on the output ages and masses. For this reason, a careful consideration of GSP-Spec's flags on the atmospheric parameters is necessary, according to the user's objectives, in order to chose the parameters with the desired reliability (see Table 2 in Recio-Blanco et al. 2023). Furthermore, close binaries and multiple stellar systems of moderate mass ratios, not caught by the RUWE parameter, may hamper our results despite the good GSP-Spec flags. These systems, the number of which is found to be anti-correlated with metallicity (e.g. Moe et al. 2019; El-Badry & Rix 2019; Price-Whelan et al. 2020), have brighter magnitudes (up to ~ -0.75 mag, in the case of an unresolved binary system of two identical stars; see Gaia Collaboration 2018b), which usually results, for a target located before the turn-off, in an overestimation of its age (and vice versa if the star is located after the turn-off; see the behaviour of the isochrones in the upper and lower panels 2 of Fig. 1).

Tests made comparing our ages and masses with reference catalogues of field stars, open clusters, and globular clusters suggest that our code performs well, provided a filtering on the estimated relative age uncertainty (we suggest <50 per cent), except for the older giants, whose ages tend to be underestimated. Ages are found to be the most reliable for turn-off stars, even when the GSP-Spec parameters have large uncertainties, whereas age estimations for giants and main-sequence stars are also retrieved reliably (with uncertainties of the order of 2 Gyr) provided the extinction towards the star's line of sight is less than $A_V \lesssim 2.5$ mag. Initial stellar masses are retrieved robustly for main-sequence and turn-off stars (dispersions compared to literature values are of the order of 0.1 $M_\odot$), whereas a filtering based on the age uncertainty of the giants is necessary to obtain reliable masses for the latter (dispersions compared to the literature values are of the order of $0.3 M_\odot$).

We complete our catalogue with galactocentric positions and velocities as well as orbital parameters (actions, eccentricities, apocentres, pericentres, maximum distance from the Galactic plane) evaluated for the entire RVS sample, using an axisymmetric Galactic potential and commonly used orbital derivation methods and codes. The catalogue, which is publicly available[12], is described in Table A.1.

Acknowledgements. We thank the referee for a constructive interaction and report. M. Fouesneau and V. Hill are warmly thanked for valuable comments, as well as CU8 and CU9 members that helped validating the stellar parameters used in this paper. This work has made use of data from the European Space Agency (ESA) mission *Gaia* (https://www.cosmos.esa.int/gaia), processed by the *Gaia* Data Processing and Analysis Consortium (DPAC, https://www.cosmos.esa.int/web/gaia/dpac/consortium). Funding for the DPAC has been provided by national institutions, in particular the institutions participating in the *Gaia* Multilateral Agreement. This research made use of Astropy, a community-developed core Python package for Astronomy (Astropy Collaboration 2013, 2018). The Centre National de la Recherche Scientifique (CNRS) and its SNO *Gaia* of the Institut des Sciences de l'Univers (INSU), its Programmes Nationaux: Cosmologie et Galaxies (PNCG) are thanked for their valuable financial support. ARB, GK and ES acknowledge funding from the European Union's Horizon 2020 research and innovation program under SPACE-H2020 grant agreement number 101004214 (EXPLORE project). PM acknowledges support from the Swedish National Space Agency (SNSA) under grant 20/136. GK gratefully acknowledges support from the french national research agency (ANR) funded project MWDisc (ANR-20-CE31-0004).

[12] http://www.astropy.org

References

Anders, F., Khalatyan, A., Chiappini, C., et al. 2019, A&A, 628, A94
Andrae, R., Fouesneau, M., Creevey, O., et al. 2018, A&A, 616, A8
Andrae, R., Fouesneau, M., Sordo, R., et al. 2023, A&A, in press, https://doi.org/10.1051/0004-6361/202243462
Astropy Collaboration (Robitaille, T. P., et al.) 2013, A&A, 558, A33
Astropy Collaboration (Price-Whelan, A. M., et al.) 2018, AJ, 156, 123
Aumer, M., & Binney, J. J. 2009, MNRAS, 397, 1286
Bailer-Jones, C. A. L. 2015, PASP, 127, 994
Bailer-Jones, C. A. L., Andrae, R., Arcay, B., et al. 2013, A&A, 559, A74
Bailer-Jones, C. A. L., Rybizki, J., Fouesneau, M., Demleitner, M., & Andrae, R. 2021, AJ, 161, 147
Basu, S., & Antia, H. M. 1997, MNRAS, 287, 189
Belokurov, V., Erkal, D., Evans, N. W., Koposov, S. E., & Deason, A. J. 2018, MNRAS, 478, 611
Bennett, M., & Bovy, J. 2019, MNRAS, 482, 1417
Bensby, T., Feltzing, S., & Oey, M. S. 2014, A&A, 562, A71
Bergemann, M., Ruchti, G. R., Serenelli, A., et al. 2014, A&A, 565, A89
Binney, J. 2012, MNRAS, 426, 1324
Binney, J., Burnett, B., Kordopatis, G., et al. 2014, MNRAS, 437, 351
Bonifacio, P., Monai, S., & Beers, T. C. 2000, AJ, 120, 2065
Bovy, J. 2015, ApJS, 216, 29
Bovy, J., Leung, H. W., Hunt, J. A. S., et al. 2019, MNRAS, 490, 4740
Bressan, A., Marigo, P., Girardi, L., et al. 2012, MNRAS, 427, 127
Caffau, E., Ludwig, H. G., Steffen, M., Freytag, B., & Bonifacio, P. 2011, Sol. Phys., 268, 255
Cantat-Gaudin, T., Anders, F., Castro-Ginard, A., et al. 2020, A&A, 640, A1
Cardelli, J. A., Clayton, G. C., & Mathis, J. S. 1989, ApJ, 345, 245
Carraro, G., Barbon, R., & Boschetti, C. S. 2002, MNRAS, 336, 259
Casagrande, L., Schönrich, R., Asplund, M., et al. 2011, A&A, 530, A138
Castro-Ginard, A., McMillan, P. J., Luri, X., et al. 2021, A&A, 652, A162
Chen, Y., Bressan, A., Girardi, L., et al. 2015, MNRAS, 452, 1068
Creevey, O. L., Sordo, R., Pailler, F., et al. 2023, A&A, in press, https://doi.org/10.1051/0004-6361/202243688
Delchambre, L., Bailer-Jones, C. A. L., Bellas-Velidis, I., et al. 2023, A&A, in press, https://doi.org/10.1051/0004-6361/202243423
Demarque, P., Woo, J.-H., Kim, Y.-C., & Yi, S. K. 2004, ApJS, 155, 667
Dotter, A. 2016, ApJS, 222, 8
Dotter, A., Chaboyer, B., Jevremović, D., et al. 2008, ApJS, 178, 89
Edvardsson, B., Andersen, J., Gustafsson, B., et al. 1993, A&A, 275, 101
El-Badry, K., & Rix, H.-W. 2019, MNRAS, 482, L139
Feuillet, D. K., Frankel, N., Lind, K., et al. 2019, MNRAS, 489, 1742
Feuillet, D. K., Feltzing, S., Sahlholdt, C. L., & Casagrande, L. 2020, MNRAS, 497, 109
Fitzgerald, M. P. 1968, AJ, 73, 983
Fouesneau, M., Andrae, R., Sordo, R., & Dharmawardena, T. 2022, dustapprox https://github.com/mfouesneau/dustapprox
Fouesneau, M., Frémat, Y., Andrae, R., et al. 2023, A&A, in press, https://doi.org/10.1051/0004-6361/202243919
Freeman, K., & Bland-Hawthorn, J. 2002, ARA&A, 40, 487
Gaia Collaboration (Prusti, T., et al.) 2016a, A&A, 595, A1
Gaia Collaboration (Brown, A., et al.) 2016b, A&A, 595, A2
Gaia Collaboration (Brown, A., et al.) 2018a, A&A, 616, A1
Gaia Collaboration (Babusiaux, C., et al.) 2018b, A&A, 616, A10
Gaia Collaboration (Helmi, A., et al.) 2018c, A&A, 616, A12
Gaia Collaboration (Brown, A., et al.) 2021a, A&A, 649, A1
Gaia Collaboration (Antoja, T., et al.) 2021a, A&A, 649, A8
Gaia Collaboration (Recio-Blanco, A., et al.) 2023a, A&A, in press, https://doi.org/10.1051/0004-6361/202243511
Gaia Collaboration (Schultheis, M., et al.) 2023b, A&A, in press, https://doi.org/10.1051/0004-6361/202243283
Gaia Collaboration (Vallenari, A., et al.) 2023c, A&A, in press,https://doi.org/10.1051/0004-6361/202243940
GRAVITY Collaboration (Abuter, R., et al.) 2020, A&A, 636, L5
Green, G. 2018, J. Open Source Softw., 3, 695
Green, G. M., Schlafly, E., Zucker, C., Speagle, J. S., & Finkbeiner, D. 2019, ApJ, 887, 93
Hayden, M. R., Bovy, J., Holtzman, J. A., et al. 2015, ApJ, 808, 132
Hayden, M. R., Recio-Blanco, A., de Laverny, P., Mikolaitis, S., & Worley, C. C. 2017, A&A, 608, L1
Haywood, M., Di Matteo, P., Lehnert, M. D., et al. 2018, ApJ, 863, 113
Helmi, A., Babusiaux, C., Koppelman, H. H., et al. 2018, Nature, 563, 85
Hidalgo, S. L., Pietrinferni, A., Cassisi, S., et al. 2018, ApJ, 856, 125
Jørgensen, B. R., & Lindegren, L. 2005, A&A, 436, 127
Kalberla, P. M. W., & Kerp, J. 2009, ARA&A, 47, 27
Kharchenko, N. V., Piskunov, A. E., Schilbach, E., Röser, S., & Scholz, R. D. 2013, A&A, 558, A53

Kordopatis, G., Recio-Blanco, A., de Laverny, P., et al. 2011, A&A, 535, A107
Kordopatis, G., Hill, V., Irwin, M., et al. 2013, A&A, 555, A12
Kordopatis, G., Binney, J., Gilmore, G., et al. 2015a, MNRAS, 447, 3526
Kordopatis, G., Wyse, R. F. G., Gilmore, G., et al. 2015b, A&A, 582, A122
Kordopatis, G., Amorisco, N. C., Evans, N. W., Gilmore, G., & Koposov, S. E. 2016, MNRAS, 457, 1299
Kordopatis, G., Recio-Blanco, A., Schultheis, M., & Hill, V. 2020, A&A, 643, A69
Lallement, R., Vergely, J. L., Valette, B., et al. 2014, A&A, 561, A91
Laporte, C. F. P., Belokurov, V., Koposov, S. E., Smith, M. C., & Hill, V. 2020, MNRAS, 492, L61
Leung, H. W., & Bovy, J. 2019, MNRAS, 483, 3255
Lindegren, L. 2018, Re-normalising the Astrometric chi-square in Gaia DR2, GAIA-C3-TN-LU-LL-124
Luri, X., Brown, A. G. A., Sarro, L. M., et al. 2018, A&A, 616, A9
Mackereth, J. T., & Bovy, J. 2018, PASP, 130, 114501
Magrini, L., Randich, S., Kordopatis, G., et al. 2017, A&A, 603, A2
Magrini, L., Spina, L., Randich, S., et al. 2018, A&A, 617, A106
Marigo, P., Bressan, A., Nanni, A., Girardi, L., & Pumo, M. L. 2013, MNRAS, 434, 488
McMillan, P. J. 2017, MNRAS, 465, 76
McMillan, P. J., Kordopatis, G., Kunder, A., et al. 2018, MNRAS, 477, 5279
Miglio, A., Chiappini, C., Morel, T., et al. 2013, MNRAS, 429, 423
Minchev, I., Chiappini, C., & Martig, M. 2013, A&A, 558, A9
Moe, M., Kratter, K. M., & Badenes, C. 2019, ApJ, 875, 61
Myeong, G. C., Vasiliev, E., Iorio, G., Evans, N. W., & Belokurov, V. 2019, MNRAS, 488, 1235
Naidu, R. P., Conroy, C., Bonaca, A., et al. 2020, ApJ, 901, 48
O'Donnell, J. E. 1994, ApJ, 422, 158
Pastorelli, G., Marigo, P., Girardi, L., et al. 2020, MNRAS, 498, 3283
Pinsonneault, M. H., Elsworth, Y. P., Tayar, J., et al. 2018, ApJS, 239, 32
Price-Whelan, A. M., Hogg, D. W., Rix, H.-W., et al. 2020, ApJ, 895, 2
Queiroz, A. B. A., Anders, F., Santiago, B. X., et al. 2018, MNRAS, 476, 2556
Recio-Blanco, A., de Laverny, P., Kordopatis, G., et al. 2014, A&A, 567, A5
Recio-Blanco, A., de Laverny, P., Palicio, P. A., et al. 2023, A&A, in press, https://doi.org/10.1051/0004-6361/202243750
Reid, M. J., & Brunthaler, A. 2020, ApJ, 892, 39
Riello, M., de Angeli, F., Evans, D. W., et al. 2021, VizieR Online Data Catalog: J/A+A/649/A3
Rosenfield, P., Marigo, P., Girardi, L., et al. 2016, ApJ, 822, 73
Salaris, M., Chieffi, A., & Straniero, O. 1993, ApJ, 414, 580
Sanders, J. L., & Binney, J. 2016, MNRAS, 457, 2107
Sanders, J. L., & Das, P. 2018, MNRAS, 481, 4093
Santos-Peral, P., Recio-Blanco, A., Kordopatis, G., Fernández-Alvar, E., & de Laverny, P. 2021, A&A, 653, A85
Schlegel, D. J., Finkbeiner, D. P., & Davis, M. 1998, ApJ, 500, 525
Schönrich, R., & Binney, J. 2009, MNRAS, 396, 203
Schönrich, R., McMillan, P., & Eyer, L. 2019, MNRAS, 487, 3568
Schultheis, M., Kordopatis, G., Recio-Blanco, A., et al. 2015, A&A, 577, A77
Schultheis, M., Rojas-Arriagada, A., García Pérez, A. E., et al. 2017, A&A, 600, A14
Skrutskie, M. F., Cutri, R. M., Stiening, R., et al. 2006, AJ, 131, 1163
Soderblom, D. R. 2010, ARA&A, 48, 581
Stello, D., Saunders, N., Grunblatt, S., et al. 2022, MNRAS, 512, 1677
Tang, J., Bressan, A., Rosenfield, P., et al. 2014, MNRAS, 445, 4287
Valentini, M., Chiappini, C., Bossini, D., et al. 2019, A&A, 627, A173
VandenBerg, D. A., Brogaard, K., Leaman, R., & Casagrande, L. 2013, ApJ, 775, 134
Zhao, H., Schultheis, M., Recio-Blanco, A., et al. 2021, A&A, 645, A14
Zwitter, T., Matijevič, G., Breddels, M. A., et al. 2010, A&A, 522, A54

Appendix A: Output catalogue format

Table A.1. Description of the columns of the published catalogue

Name of column	Description	Units
source_id	Gaia DR3 source ID	–
age	Inferred age	Gyr
age_error	Uncertainty on the inferred age	Gyr
m_ini	Inferred initial stellar mass	$M_\odot$
m_ini_error	Inferred uncertainty on the initial stellar mass	$M_\odot$
teff	Adopted projected $T_{\rm eff}$	K
logg	Adopted projected $\log g$	dex
meta	Adopted projected [M/H]	dex
p_flavour	Adopted projection flavour for inferred ages and masses	
G	Inferred absolute G magnitude	mag
G_BP	Inferred absolute G_{BP} magnitude	mag
G_RP	Inferred absolute G_{RP} magnitude	mag
ebprp	Inferred reddening using the projected G_{BP} and G_{RP}	mag
ebprp_error	Uncertainty on the inferred reddening	mag
**_spec	Parameters adopting the calibrated GSP-Spec parameters only	
**_speck	Parameters adopting the calibrated GSP-Spec parameters and the K_s absolute magnitude	
**_specjhk	Parameters adopting the calibrated GSP-Spec parameters and the J, H, K_s absolute magnitudes	
**_specjhkg	Parameters adopting the calibrated GSP-Spec parameters and the J, H, K_s, G absolute magnitudes	
x_med_dgeo	Median galactocentric Cartesian X position	kpc
y_med_dgeo	Median galactocentric Cartesian Y position	kpc
z_med__dgeo	Median galactocentric Cartesian Z position	kpc
r_med_dgeo	Median heliocentric line-of-sight distance with geometric prior from Bailer-Jones et al. (2021)	pc
vr_med_dgeo	Median galactocentric radial velocity obtained using r_med_dgeo	km s^{-1}
vphi_med_dgeo	Median galactocentric azimuthal velocity obtained using r_med_dgeo	km s^{-1}
vz_med_dgeo	Median galactocentric vertical velocity obtained using r_med_dgeo	km s^{-1}
jr_med_dgeo	Median radial action obtained using r_med_dgeo	kpc km s^{-1}
jphi_med_dgeo	Median angular momentum (i.e. azimuthal action) obtained using r_med_dgeo	kpc km s^{-1}
jz_med_dgeo	Median vertical action obtained using r_med_dgeo	kpc km s^{-1}
zmax_med_dgeo	Median maximum distance from the galactic plane obtained using r_med_dgeo	kpc
rapo_med_dgeo	Median apogalactic radius reached by the star, obtained using r_med_dgeo	kpc
rperi_med_dgeo	Median perigalactic radius reached by the star, obtained using r_med_dgeo	kpc
e_med_dgeo	Median eccentricity, obtained using r_med_dgeo	kpc
**_upper_dgeo	Upper confidence limit of the parameters	
**_lower_dgeo	Lower confidence limit of the parameters	
**_dphotogeo	Parameters obtained using the photogeometric distances from Bailer-Jones et al. (2021)	

Appendix B: Results of the isochrone projection with extinction

Figures B.1 to B.3 are similar to Fig. 3. They consider only the `speck`, `specjhk`, and `specjhkg` projections, with Q50 uncertainties in $T_{\rm eff}$, $\log g$, and [M/H], and uncertainties in J, H, K_s, and G, as indicated in the top left corner of each plot. The input magnitudes are reddened according to the extinction A_V labelled within each plot.

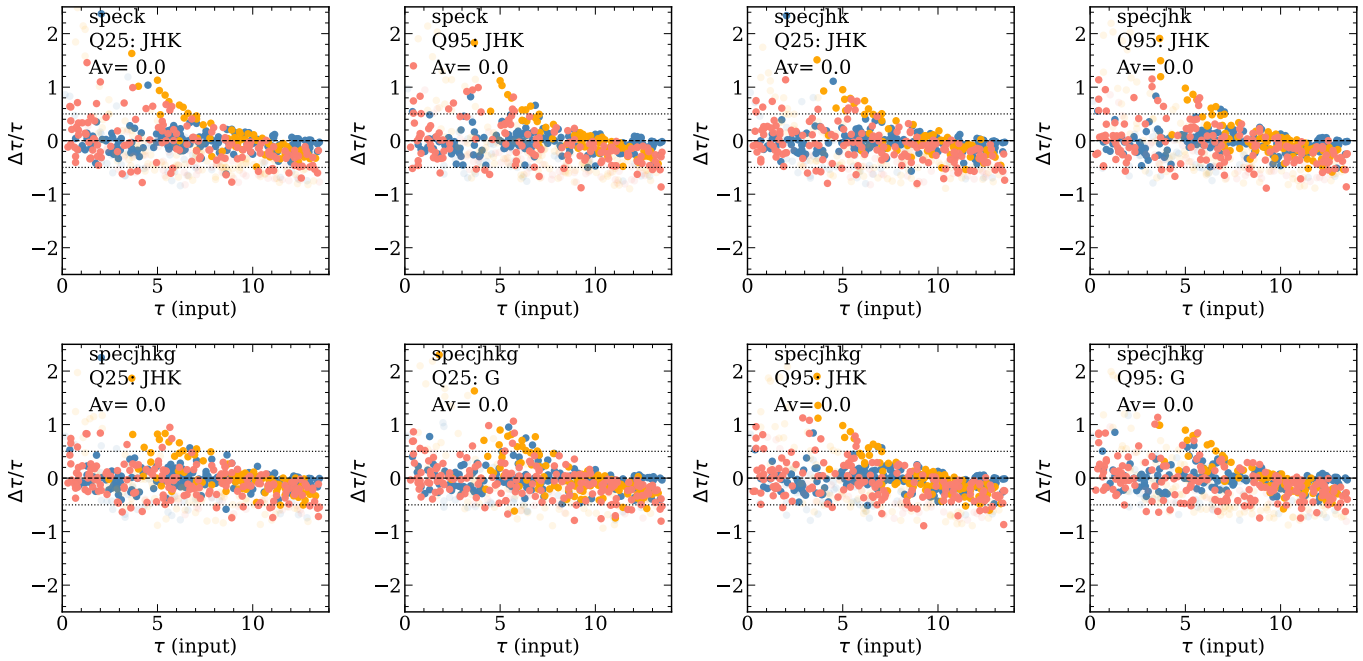

Fig. B.1. Comparison of the input ages vs the relative error of the output ones, for the `speck`, `specjhk`, and `specjhkg` projections, with Q50 uncertainties in $T_{\rm eff}$, $\log g$, and [M/H], and uncertainties in J, H, K_s, and G as indicated in the top left corner of each plot. No interstellar extinction is considered here.

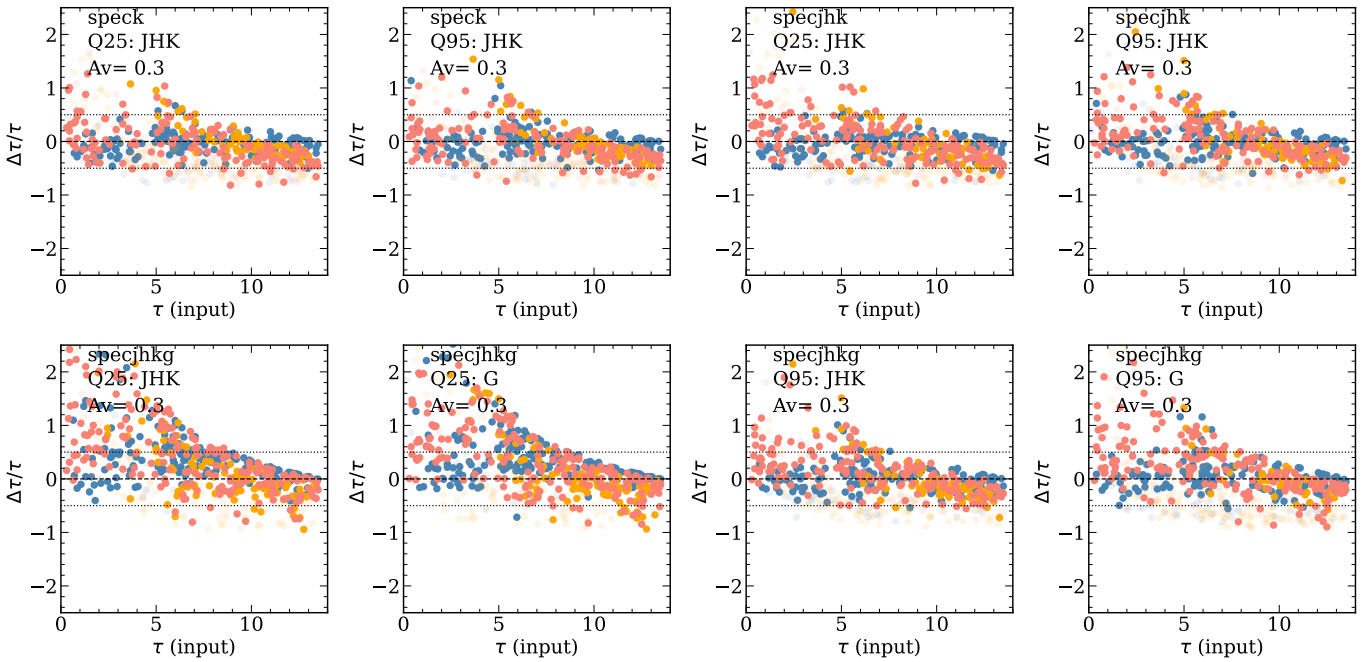

Fig. B.2. Similar to Fig. B.1, but with an extinction of $A_V = 0.3$ mag.

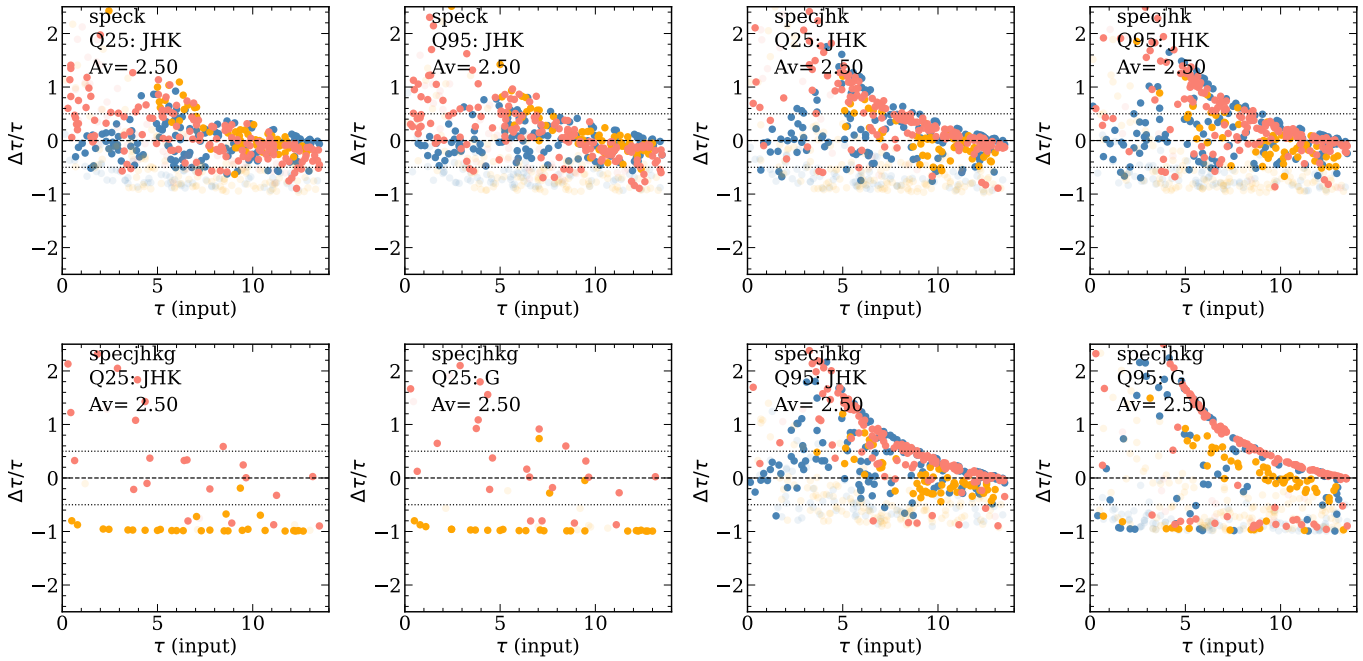

Fig. B.3. Similar to Fig. B.1, but with an extinction of $A_V = 2.5$ mag.

Appendix C: Open and globular cluster plots

Figures C.1 and C.2 show open and globular cluster targets, in the $T_{\rm eff}$-log g and $T_{\rm eff}$-$M_{\rm K_s}$ spaces. In red are plotted the isochrones with metallicity and age equal to the mean GSP-Spec (calibrated) metallicity and mean derived age of the cluster stars, whereas in black we plot the isochrones for the reference age.

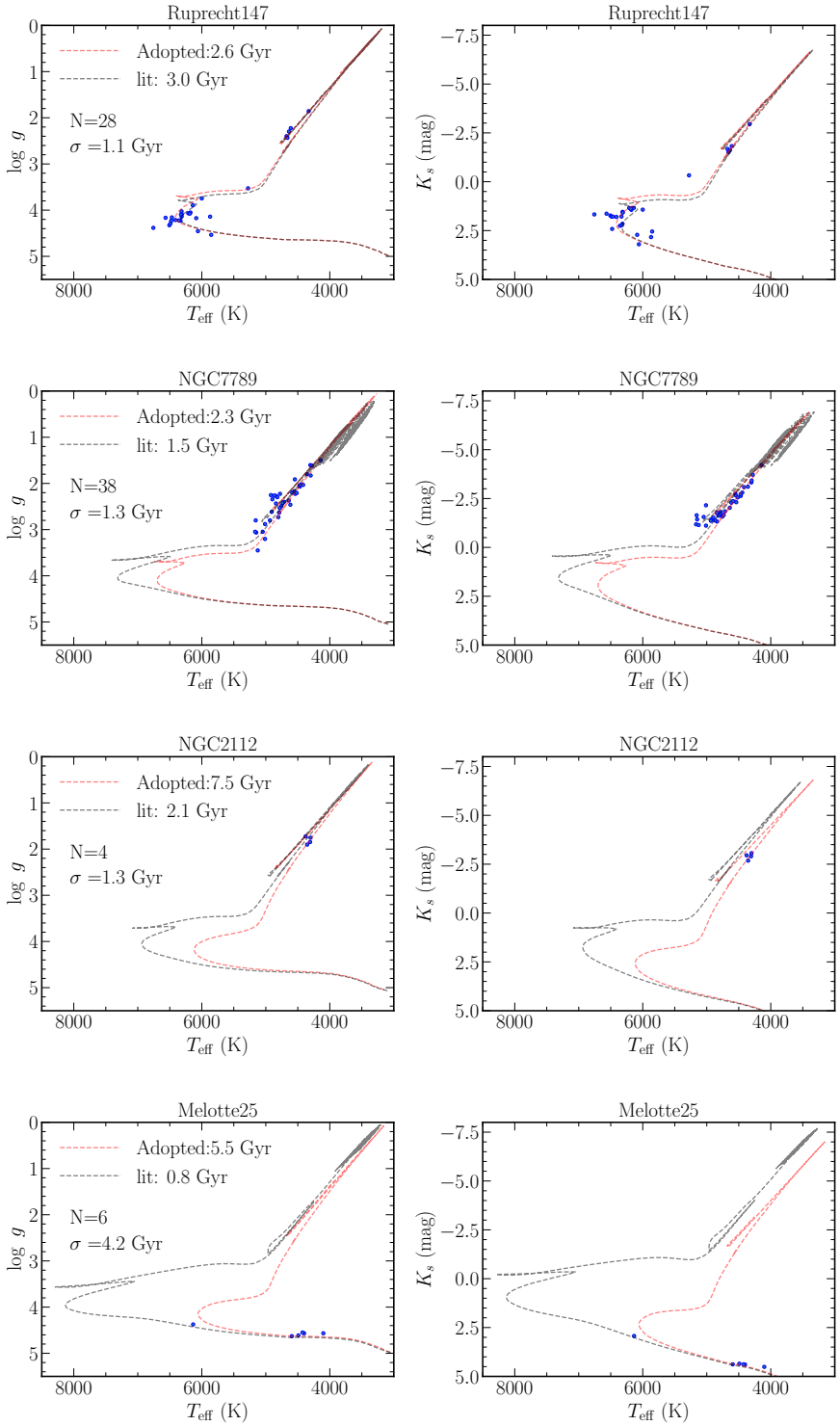

Fig. C.1. $T_{\rm eff}$-log g (left) and $T_{\rm eff}$-$M_{\rm K_s}$ (right) diagrams for a few cherry-picked open clusters. The isochrones of the adopted mean age (in red) and the reference age from Cantat-Gaudin et al. (2020) are plotted in red and black, respectively, for the mean metallicity of the cluster derived from the calibrated GSP-Spec values. The first two rows show examples for which our ages and the literature values are in good agreement. The bottom two rows show the opposite: for NGC2112 our solution fits the data better than the younger isochrone, pointing towards offsets in the input $T_{\rm eff}$, [M/H], or distance modulus. For NGC7789, our solution is not reliable, since main-sequence stars do not constrain the ages well enough.

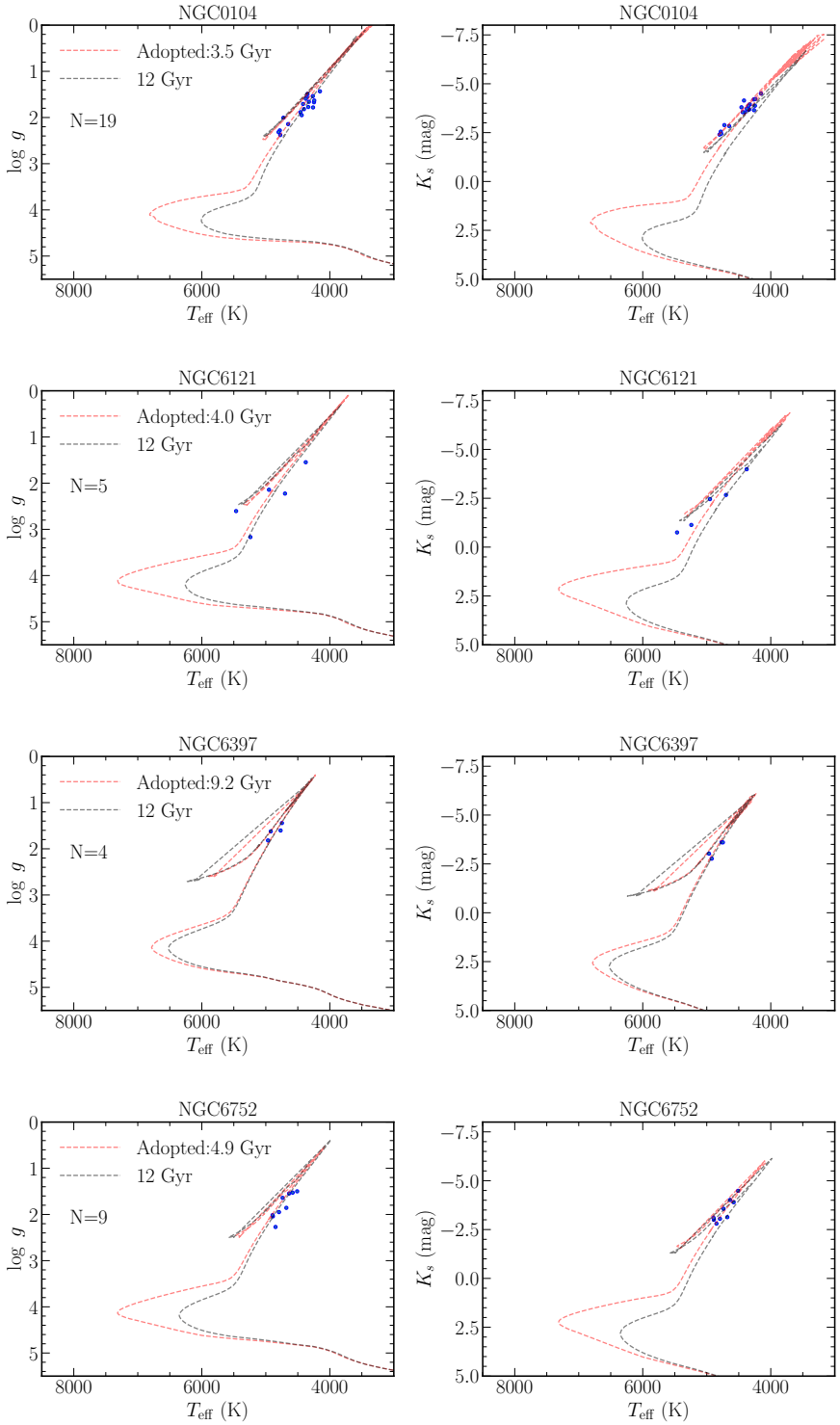

Fig. C.2. $T_{\rm eff}$-log g (left) and $T_{\rm eff}$-$M_{\rm K_s}$ (right) diagrams for a few cherry-picked globular clusters. Candidate stars were selected based on the results of Gaia Collaboration (2018c). The isochrones with the adopted mean age (in red) and for 12 Gyr are plotted in red and black, respectively, for the mean metallicity of the cluster derived from the calibrated GSP-Spec values.